Biosensors and Bioelectronics 160 (2020) 112220

Contents lists available at ScienceDirect

Biosensors and Bioelectronics

journal homepage: http://www.elsevier.com/locate/bios

Highly flexible and conductive poly (3, 4-ethylene dioxythiophene)-poly (styrene sulfonate) anchored 3-dimensional porous graphene network-based electrochemical biosensor for glucose and pH detection in human perspiration

Md Abu Zahed, Sharat Chandra Barman, Partha Sarati Das, Md Sharifuzzaman, Hyo Sang Yoon, Sang Hyuk Yoon, Jae Yeong Park *

Micro/Nano Devices and Packaging (MiNDaP) Laboratory, Department of Electronic Engineering, Kwangwoon University, Seoul, Republic of Korea

ARTICLE INFO

Keywords:
PEDOT:PSS
Laser-induced graphene
Flexible biosensor
Glucose and pH detection
Human perspiration

ABSTRACT

The patterned LIG flakes are generally not interconnected due to the line gap of the laser ray, leading to lower uniform conductivity and fragile graphene. Thus, the fabrication of a highly conductive and mechanically robust LIG-based biosensing platform remains challenging. In this study, the fabrication of a flexible electrochemical biosensor is reported based on poly (3, 4-ethylene dioxythiophene)-poly (styrene sulfonate) (PEDOT:PSS) modified 3-dimensional (3D) stable porous laser-induced graphene (LIG) for the detection of glucose and pH. PEDOT:PSS was spray-coated on the LIG to improve electrode robustness and deliver uniform electrical conductivity. The as-prepared PEDOT:PSS modified LIG (PP/LIG) was characterized using field-emission scanning electron microscopy (FESEM), x-ray photoelectron spectroscopy (XPS), Raman spectroscopy, and Fourier-transform infrared spectroscopy (FTIR). Platinum and palladium nanoparticles (Pt@Pd) were successfully electrodeposited on PP/LIG, markedly enhancing the electrocatalytic activity for glucose detection. The fabricated biosensor exhibited an excellent amperometric response to glucose with a wide linear range of 10 μM − 9.2 mM, a high sensitivity of 247.3 $\mu AmM^{-1}cm^{-2}$, and a low detection limit (LOD) of 3 μM, with high selectivity. In addition, the pH sensor was functionalized by the polyaniline (PANI) on PP/LIG, and it also exhibited excellent potentiometric response with a high sensitivity of 75.06 mV/pH in the linear range of pH 4 − 7. Ultimately, the feasibility of the biosensor was confirmed by the analysis of human perspiration collected during physical exercise. This approach validates the utility of the novel fabrication procedure, and the potential of the LIG-conductive polymer composite for biosensing applications.

1. Introduction

Diabetes is a prevalent chronic disease caused by inadequate insulin secretion, which hinders the capability of cells to absorb glucose from the blood(Whiting et al., 2011)(Newman and Turner, 2005). Patients with diabetes are recommended to monitor their blood glucose levels daily and to take oral medication, and insulin regimen for maintaining stable glycemic control (Collaborators, 1991). Human perspiration is an intrinsic body fluid that offers valuable information about an individual's health and fitness based on the levels of several metabolites, such as lactate, and glucose, as well as electrolytes, and pH levels (Sonner et al., 2015)(Imani et al., 2016). Sweat glucose levels can accurately reflect blood glucose levels, with a correlation whereby 0.3 mM glucose in sweat corresponds to 16.7 mM glucose in the blood (Moyer et al., 2012). Besides, pH plays an important role in the pathogenesis of skin diseases like acne vulgaris, ichthyosis, and candida albicans infections (Schmid-Wendtner and Korting, 2006). Changes in sweat pH levels can provide valuable information regarding atopic dermatitis, and fungal infections (Patterson et al., 2000)(Bandodkar et al., 2013). Furthermore, type II diabetes patients with kidney stones are reported to exhibit lower than normal sweat pH (Nyein et al., 2016) Therefore, the accurate measurement of glucose and pH level in sweat is necessary for the assessment of certain health conditions.

Flexible biosensing devices that can be laminated onto the human

* Corresponding author.
E-mail address: jaepark@kw.ac.kr (J.Y. Park).

https://doi.org/10.1016/j.bios.2020.112220
Received 6 February 2020; Received in revised form 6 April 2020; Accepted 15 April 2020
Available online 20 April 2020

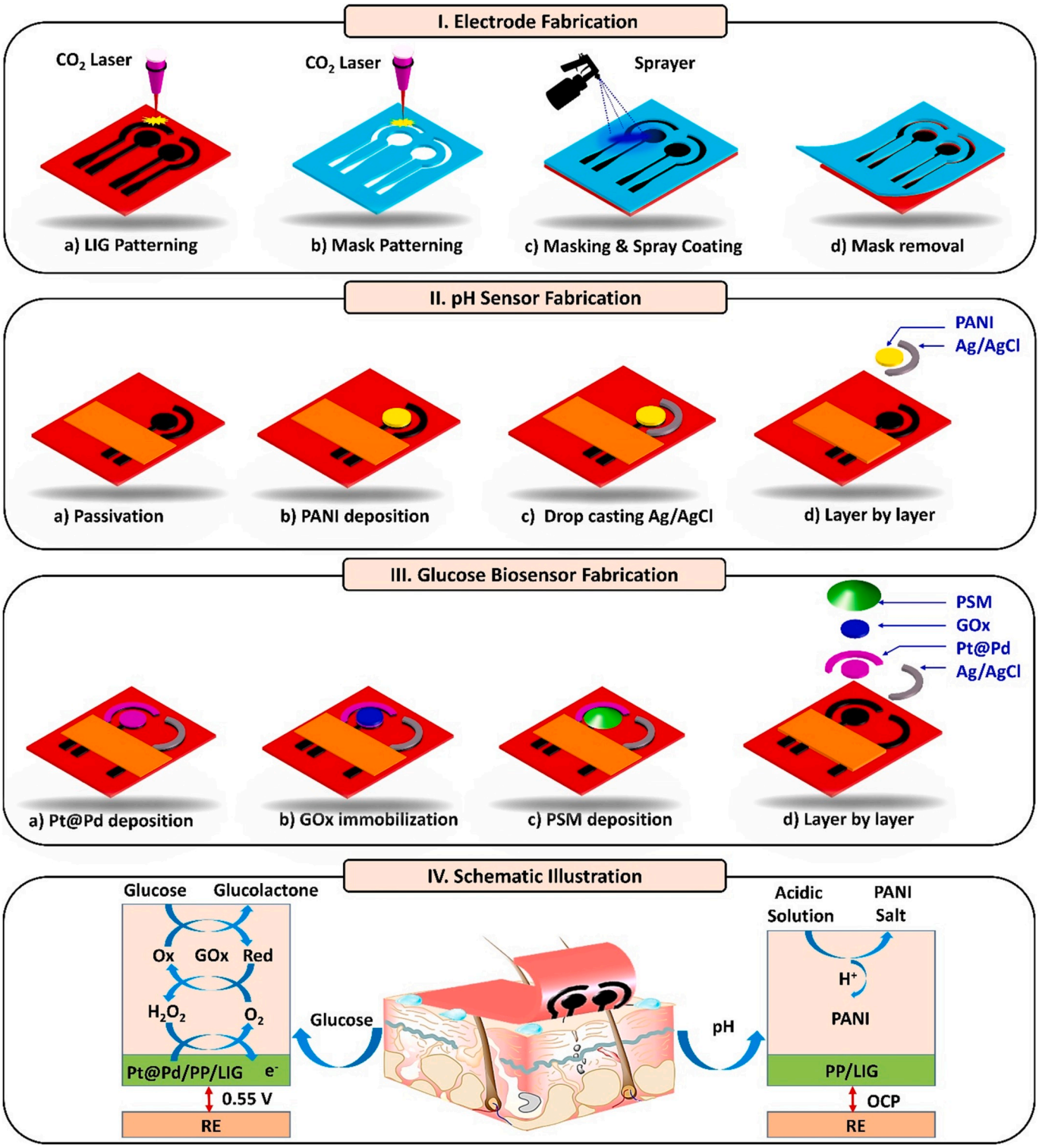

Fig. 1. Fabrication procedure of the biosensor. I) Electrode fabrication steps. I.a) LIG patterning for electrodes, I.b) Laser cutting of a PI tape, I.c) Electrodes masking and spray coating of PEDOT:PSS, I.d) Manual mask removal. II) pH sensor fabrication procedure. II.a) Passivation layer formation, II.b) PANI deposition on the working electrode, II.c) Ag/AgCl paste on the reference electrode (RE), II.d) Layer by layer representation of the pH sensor. III) Glucose biosensor fabrication. III.a) Electrodeposition of Pt@Pd nanoparticles on the working and counter electrodes, III.b) GOx immobilization III.c) Permiselective membrane (PSM) layer deposition, III.d) All layers of the glucose biosensor. IV) Schematic illustration of the whole device.

skin to continuously monitor the physiological biomarkers have drawn tremendous attention in both academia and industry (Guo et al., 2017) (Gao et al., 2016). At present, flexible electrochemical biosensors present a promising approach for the noninvasive monitoring of biomolecules from sweat, owing to their unique advantages of sensor miniaturization, high sensitivity, and label-free direct measurement (Matzeu et al., 2015)(Bandodkar et al., 2016). Various types of flexible electrochemical biosensors have been reported for the monitoring of biomolecules in sweat. However, the majority require complicated and multistep fabricating processes, such as chemical vapor deposition

(Munje et al., 2017), photolithography (Lei et al., 2019), and screen printing (Abellán-Llobregat et al., 2017), which hinders mass-production of multi-analytes sensing platforms.

Recently, LIG has been introduced as an excellent active material for use in flexible electrochemical devices, such as energy storage and sensor devices, because of its simple fabrication procedure and a large surface area (~340 m^2/g) (Barman et al., 2020)(Nayak et al., 2016). Direct CO_2 laser patterning on flexible polyimide film is a one-step, cost-effective and scalable method for ablating 3D porous LIG, where sp^3-carbon atoms of the film are thermally reshaped to sp^2-carbon atoms (Lin et al., 2014)(Kurra et al., 2019). However, using LIG in biomedical applications is challenging owing to its poor robustness. Moreover, recurrent bending leads to structural deformation of the graphene flakes, thereby deteriorating electrical performance.

PEDOT:PSS, a well-known conductive polymer, has been applied in the biomedical field owing to several unique advantages, such as its good electrical conductivity, chemical stability, solution processibility and favorable biocompatibility (Takamatsu et al., 2015)(Brugarolas et al., 2016). Nonetheless, there is scope for enhancing electrical conductivity by various methods; for example by introducing the phase separation of PEDOT chains from PSS through the addition of organic co-solvents, such as dimethyl sulfoxide, glycerol, and ethylene glycol (del Agua et al., 2018)(Guo et al., 2016). There are several influential and pragmatic reasons for choosing PEDOT:PSS as an active material for the biosensing platform. Firstly, PEDOT:PSS behaves as a redox mediator toward several analytes and significantly improves the sensitivity (Setti et al., 2005). Secondly, PEDOT:PSS functions as a linker in the pores of LIG, increasing electrode robustness by the high ductility of it. Finally, the PEDOT chains firmly interconnect the graphene flakes, which enhances the electrical conductivity, and the PSS chains become intertwined on the edges of flakes.

The bimetallic nanoparticles have drawn much attention as electrocatalyst in the electrode matrix to amplify biological interactions (Zhang et al., 2007)(Zhang et al., 2010). In particular, the Pt–Pd alloy nanoparticles offer synergistic effects via cooperative interactions occurred due to the geometric and electronic effects of the nanocomposite, which enhances the electron transfer rate and better robustness against intermediate species (Hossain and Park, 2015)(Li et al., 2019). In addition, the superior properties of PANI, such as high pH-sensitive conductivity, negligible cytotoxicity, and nominal skin irritation have led to its extensive use in the production of pH sensors (Semwal and Gupta, 2019)(Patil et al., 2019).

In this research, we report the novel fabrication of an inexpensive and multifunctional LIG based flexible electrochemical biosensor for both glucose and pH sensing in human perspiration. The highly conductive and mechanically robust electrodes are newly fabricated by spray coating of co-solvent diluted PEDOT:PSS on the direct patterned LIG. The working electrodes are further modified with electroplating Pt@Pd nanoparticles for glucose detection, and with the electropolymerization of aniline for pH detection. The proposed multi-sensing device presents another step toward perspiration analysis for the continuous monitoring of physiological compounds.

2. Material and methods

2.1. Reagents and instrumentation

All reagents and apparatus, design of the electrodes are detailed in the supporting information (S 2.1 − S 2.3).

2.2. Fabrication of the flexible electrodes

For the fabrication of the electrodes, a section of commercial PI sheet was selected as the substrate. The PI sheet was cleaned sequentially by isopropyl alcohol, methanol, and deionized (DI) water. Then, a CO_2 pulsed laser (power-17 W, speed-6 cms^{-1}, optimized, details in S 2.4 and Table S1) was used to convert the PI (optimized thickness = 100 μm) into 3D porous graphene under ambient conditions, as shown as step (I. a) of the fabrication procedure (Fig. 1). The mapping and the optical image of the LIG electrodes are shown in Figs. S2A and S2B. Next, four solutions of PEDOT:PSS and ethylene glycol were prepared with a range of weight-percentages (5, 10, 15, and 20 wt %). The sonication probe (power-80 W, amplitude-50%) was applied for 30 min to ensure the thorough mixing of PEDOT:PSS and ethylene glycol. Subsequently, a shadow mask was patterned by laser (power = 100 W), using adhesive polyimide tape, as illustrated in step (I.b). The unpatterned LIG area was then covered with the shadow mask and the as-prepared solutions were spray-coated and cured at room temperature for 24 h, as shown in step (I.c). Identical parameters (time: 30s and speed: N_2 gas flow) were maintained for spray coating the various PEDOT:PSS solutions. The coating speed was controlled by N_2 gas flow. Finally, the mask was peeled off manually from the substrate to obtain the desired PEDOT:PSS/LIG (PP/LIG) electrodes depicted in step (I.d).

2.3. Preparation of the pH sensor

The fabrication procedure of the pH sensor is shown in Fig. 1(II). To passivate the sensor connections, a section of PI scotch tape was attached as depicted in step (II.a). The pH sensor consisted of two electrodes: the reference and working electrodes. To functionalize the working electrode, the PP/LIG electrode was dipped into 0.1 M aniline aqueous solution containing 1 M HCl and CV was conducted in the potential range of −0.2 to 1 V for 60 segments at a scan rate of 100 mVs^{-1}. Evidence for aniline electropolymerization is shown in Fig. S3, where the CV area increases with increasing numbers of segments. The PANI deposited working electrode is shown step (II.b). To assemble the common reference electrode for the glucose and pH sensors, a drop of Ag/AgCl paste was cast onto the PP/LIG electrode and kept at 60 °C for 30 min, as presented in step (II.c). Step (II.d) illustrates all the layers of the final pH sensor.

2.4. Preparation of the glucose biosensor

The fabrication of the glucose biosensor is depicted in Fig. 1(III). The Pt@Pd nanoparticles were electrodeposited on both the working and the counter electrodes, as shown in step (III.a). The Pt@Pd nanoparticles were electrodeposited on the working electrode by CV in the potential range of −0.1 V to −0.9 V for 20 segments in a 60 mM H_2SO_4 solution containing 2.5 mM of K_2PtCl_4 and 2.5 mM of $PdCl_2$. To generate the counter electrode, the electrodeposition was conducted with CV for 40 segments to allow facile current flow from working to counter electrode. To immobilize enzymes onto the working electrode, 8 μL water solution containing 20 mM EDC:NHS (1:1) was drop-cast onto it, the electrode was kept at room temperature for 7 h for incubation. Subsequently, 5 mg of GOx and 3 mg of chitosan were mixed with 0.6 mL DI water and stirred well for 15 min. Then, 9 μL of the as-prepared mixture was drop-cast onto it. Afterward, the enzyme-modified electrode, shown in step (III.b), was stored inside the incubator at 4 °C overnight. Nafion:DI water (1:7, 5 μL) was deposited onto the working electrode as a permiselective membrane, depicted in step (III.c). The fully-assembled sensor was then dried at room temperature for 40 min and stored at 4 °C prior to using. The layer by layer representation of the glucose biosensor is shown in step (III.d). The optical image of the fabricated final device is shown in Fig. S2C.

3. Results and discussion

3.1. Physical characterization of the modified LIG electrodes

The surface morphology, chemical interactions, and elemental analysis of Pt@Pd/PP/LIG and PANI/PP/LIG were studied by FESEM, Raman spectroscopy, XPS, and EDS. The FESEM image of the porous 3D

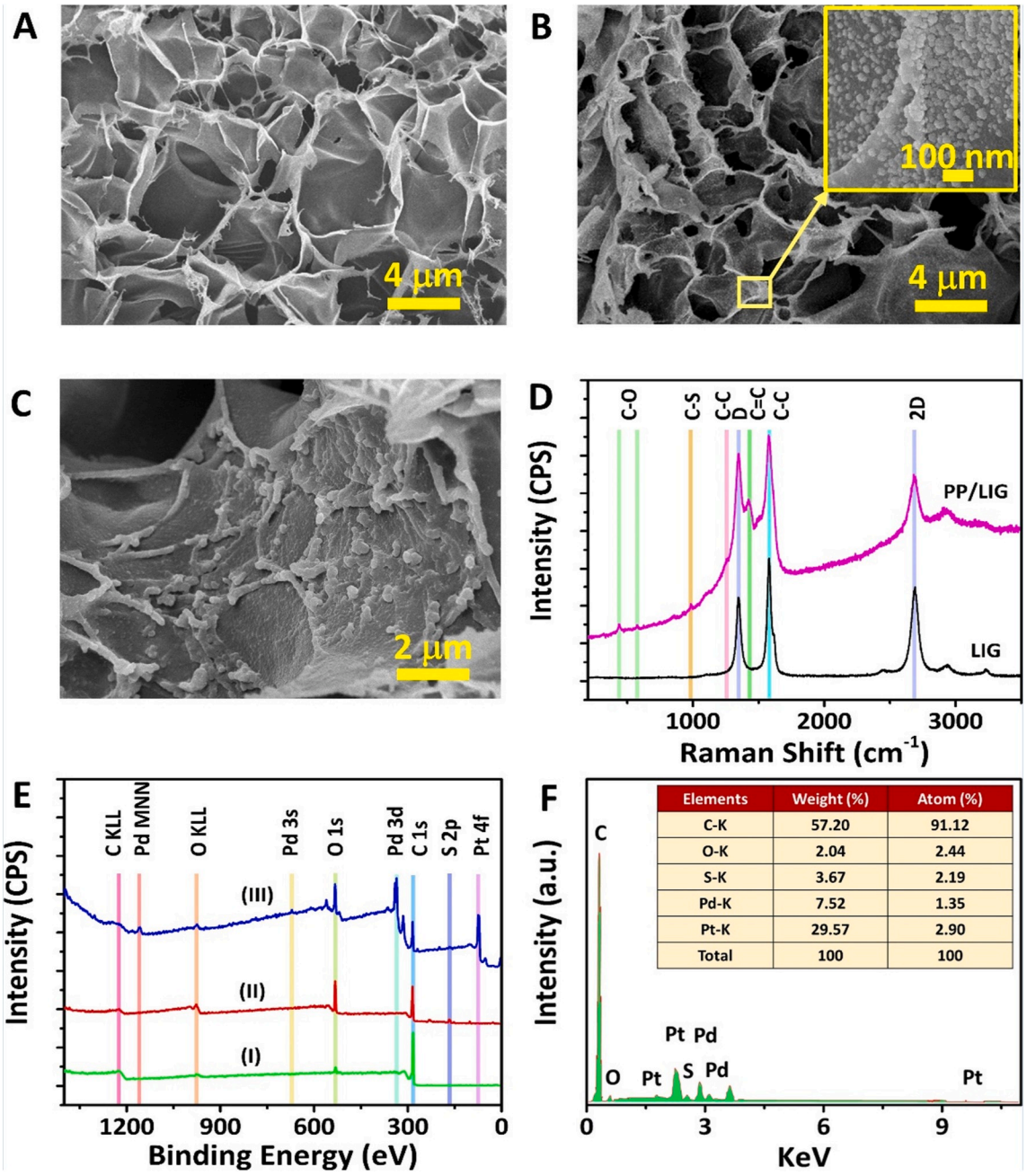

Fig. 2. FESEM images of A) bare LIG, B) Pt@Pd/PP/LIG (the inset is at high magnification showing Pt and Pd nanoparticles), and C) PANI/PP/LIG, D) Raman spectra of bare LIG and PP/LIG, E) XPS spectra of (I) bare LIG, (II) PP/LIG,(II) Pt@Pd/PP/LIG with distinct element intensity peaks, F) EDS spectra of Pt@Pd/PP/LIG (the inset table shows atom and weight percentages of Pt, Pd, O, C and S).

network of bare LIG, resulting from the expeditious release of gaseous products, is shown in Fig. 2A. This porous network facilitates the penetration of the highly conductive PEDOT:PSS polymer and provides a large electrochemically active surface area (Guangyuan Xu et al., 2018). In the case of the 5 and 10 wt% PP/LIG samples, the LIG flakes became thicker with increasing weight percentages of PEDOT:PSS, as presented in Figs. S4A and S4B. However, In the 15 wt% PP/LIG, PEDOT:PSS was not only attached to the LIG pores and flakes, but also functioned as an excellent conductive binder, interconnecting LIG flakes and resulting in a mechanically robust electrode assembly, as depicted in Fig. S4C. This is attributed to the sulfonation of the LIG flakes, which introduces negative charges that engage in strong electrostatic interactions with the positively charged PEDOT chains (Du et al., 2018). In contrast, for 20 wt % PP/LIG, PEDOT:PSS self-combined and stacked together, forming a condensed film on the surface, which is vulnerable and suffered mechanical cracks after a few bendings, resulting in an increase in electrical resistance, as depicted in Fig. S4D and Fig. S10B. The FESEM image of the optimized electrode for the glucose biosensor, fabricated using 15 wt % PEDOT:PSS and 20-segment electrodeposition of Pt@Pd nanoparticles, is given in Fig. 2B. The FESEM images (Figs. S5 and S6) for the optimization of depositing Pt@Pd nanoparticles are discussed in chapter S 3.1. For the pH sensor, PANI was deposited electrochemically onto the 15 wt% PP/LIG sample. Fig. 2C represents the FESEM image, revealing the morphology of the fabricated PANI/PP/LIG.

The chemical interactions between PEDOT:PSS and LIG were investigated by Raman spectroscopy, presented in Fig. 2D. The spectrum of bare LIG exhibits the presence of a D band at ~1349 cm^{-1}, induced by defects in the sp^2 coordinated 6-carbon atom rings. The prominent first

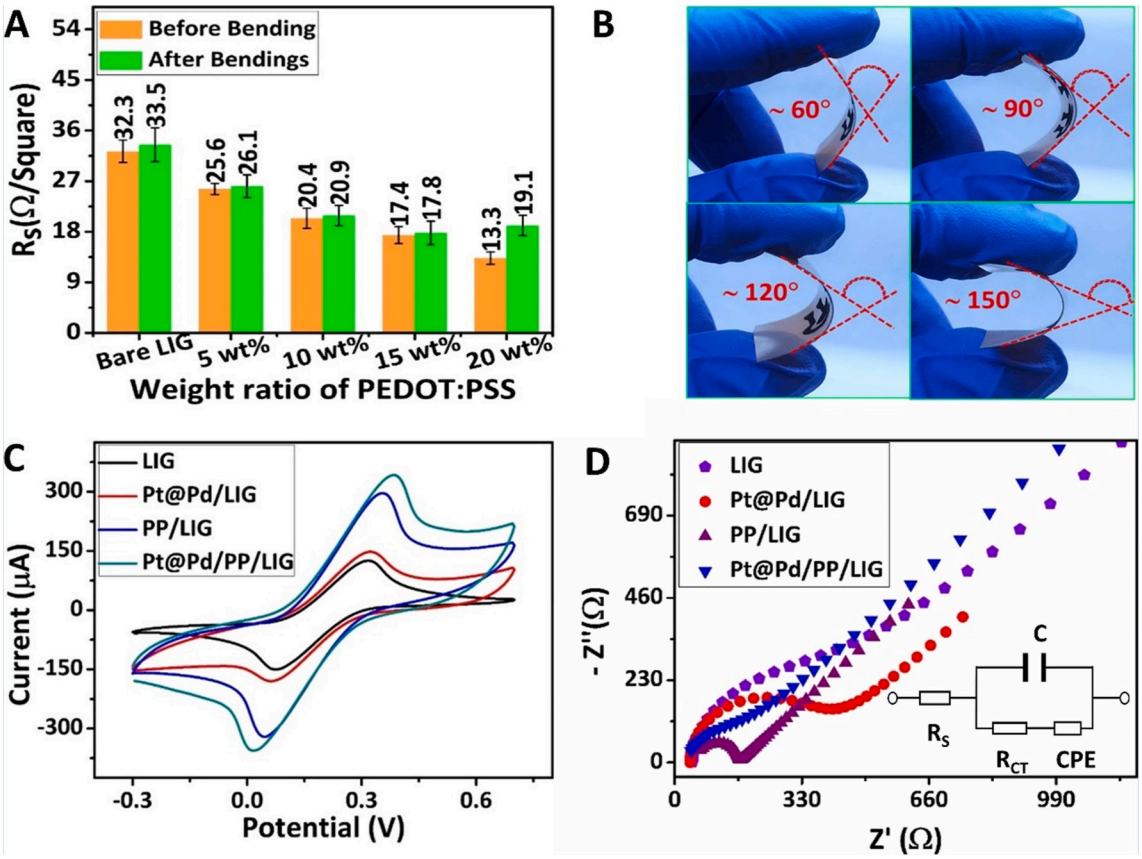

Fig. 3. A) Changes in sheet resistances (before and after bendings) of LIG electrodes modified with various weight percentages of PEDOT:PSS, B) Optical images for bending conditions of the fabricated 15 wt% PP/LIG electrode, C) CV performance analysis of bare LIG, Pt@Pd/LIG, PP/LIG, and Pt@Pd/PP/LIG, D) EIS fitted curves of bare LIG, Pt@Pd/LIG, PP/LIG, and Pt@Pd/PP/LIG (the inset shows the equivalent circuit used in EIS fitting).

order G peak at ~1581 cm^{-1} and the 2D peak at ~2695 cm^{-1} emanated from the second-order zone boundary phonons (Ferrari et al., 2006). The high intensities of I_G/I_D (3.7) and I_{2D}/I_G (0.41) were attributed to defects and multilayer structures of the graphene flakes. The conformational changes of LIG with the addition of PEDOT:PSS were evident in the Raman spectrum of PP/LIG. The spectrum contains several diagnostic peaks; C–C inter-ring stretching (~1245 cm^{-1}), single C–C bond stretching (~1556 cm^{-1}), and strong peaks arising from C═C symmetric stretching (~1431 cm^{-1}) indicating the presence of both PEDOT:PSS and LIG on the electrode (Jiang et al., 2017). The intense peak between the D and G peaks at a higher wavenumber of ~1431 cm^{-1}, results from the strong π–π interaction of LIG with PEDOT and PSS chains, which induces the phase separation of PEDOT:PSS and promotes the alignment of PEDOT on the graphene network (Links, 2012). Moreover, the FTIR spectra (Fig. S7) of LIG and PP/LIG validate the Raman results. All of the PEDOT:PSS significant peaks for S–O (945 cm^{-1}), S-phenyl (1124 cm^{-1}) bonds in sulfonic acid and C═C (1514 cm^{-1}), C–C (1270 cm^{-1}) and C–S (706 cm^{-1}) bonds in the thiophene are well visible in the PP/LIG electrode (Liu et al., 2015)(Lee and Choi, 2015). From Table S2, the Raman peaks and bonds for LIG and PP/LIG are corroborated by the FTIR peaks and bonds, indicating successful coating of PEDOT:PSS on LIG.

The XPS spectra of LIG, PP/LIG, and Pt@Pd/PP/LIG (Fig. 2E) indicated an elemental composition of predominantly carbon (C), oxygen (O), sulfur (S), platinum (Pt), and palladium (Pd). The XPS spectrum of LIG shows a dominant carbon peak over the oxygen peak. The C1s spectrum of LIG illustrates that the carbon peak of the PI film is divided into several peaks with binding energies of approximately 284.5 eV, 285.42 eV, 286.89 eV, and 288.5 eV, which are attributed to C═C, C–C, C–O, and C═O, respectively (Fig. S8A) (Zhang et al., 2018). The XPS survey spectrum of the PP/LIG indicates the presence of C1s, O1s, and S2p signals, implying that the PEDOT:PSS is chemically bonded onto the LIG pores and flakes. Furthermore, the XPS survey spectrum of Pt@Pd/PP/LIG confirmed the existence of all surface chemical elements through their distinctive peaks. The high-resolution C1s spectrum (Fig. S8B) of Pt@Pd/PP/LIG contained five distinct peaks, including those arising from the aromatic C═C of PEDOT at 284.55 eV, the aliphatic C–C of the PSS chains at 285.5 eV, the C–O/C–S peaks at 286.56 eV, and the C═O/C═S peaks at 288.8 eV (Guo et al., 2013) (Merche et al., 2010). The redshifts of all the C1s peaks of the Pt@Pd/PP/LIG sample, compared to the bare LIG C1s peaks, suggested strong π–π bonding between the PEDOT chains and LIG, as well as confirming the electrostatic interaction between the hydrophilic groups of the PSS chains and LIG. The high-resolution spectrum of two major peaks in the S2p spectra (Fig. S8C), including shake-up peaks at binding energies of 163–165 eV and 167–170 eV, correspond to the sulfur signal of PEDOT and PSS moieties, respectively (Kim et al., 2018). Figs. S8D and S8E represent the XPS spectra of Pt and Pd nanoparticles electrodeposited on the PP/LIG electrode. The two asymmetric peaks for Pd 3d were attributed to $Pd_{5/2}$ and $Pd_{3/2}$, with binding energies of 335.36 eV and 340.6 eV, respectively(Choe et al., 2015). Deconvolution of the Pt 4f peaks, having binding energies of 71.19 eV and 74.52 eV, correspond to spin orbits of $4f_{7/2}$ and $4f_{5/2}$, respectively(Sharifuzzaman et al., 2019). These results proved the existence of Pt@Pd nanoparticles as well as the authenticity of CV electrodeposition. Furthermore, the elemental composition of Pt@Pd/PP/LIG was investigated through EDS mapping, as shown in Fig. 2F. The atomic percentages of C, O, S, Pd, and Pt were mapped as 91.12%, 2.44%, 2.19%, 1.35%, and 2.90%, respectively, agreeing well with the XPS results.

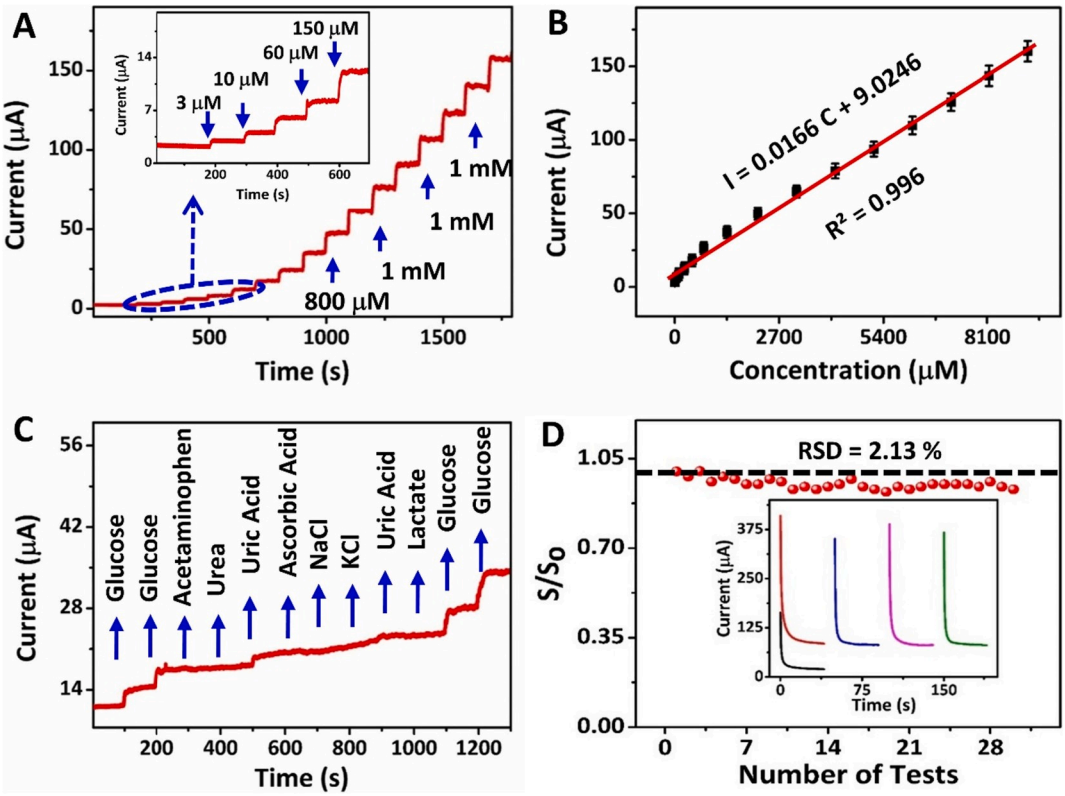

Fig. 4. Electrochemical investigation of the fabricated glucose biosensor. A) Amperometric response with a range of glucose concentrations from 3 μM to 9.2 mM, B) Calibration plot for the biosensor, C) Selectivity test of the biosensor, D) Relative responses (S/S_0) calculated from the chronoamperometry response by the ratio of instant current (S) to initial current (S_0); the inset figure shows currents in 0.1M PBS containing 1 mM glucose at the 1st (with and without I mM glucose injection), 10th, 20th, 30th test.

3.2. Electrical characterization of the PEDOT:PSS modified LIG electrodes

The electrical conductivities of the electrodes modified with various weight ratios of PEDOT:PSS were assessed form the sheet resistances measured with a four-point probe. Fig. 3A depicts the variation in sheet resistances with varying weight ratios of PEDOT:PSS. The electrical conductivities were calculated from the sheet resistance and the electrode thickness, using the following equation:

$$Electrical\ conductivity\ (S/cm) = \frac{1}{Sheet\ resistance(\Omega/cm) \times thickness(cm)} \quad (1)$$

The electrode thickness (35 μm) was deduced from the cross-section image of the electrode shown in Fig. S9. The 5 and 10 wt% of PP/LIG electrodes exhibited conductivities of 111.6 Scm^{-1} (~25.6 Ω/sq.), and 140.6 Scm^{-1} (~20.4 Ω/sq.), respectively. The conductivities were not marginally improved compared to bare LIG, owing to a lower concentration of PEDOT:PSS. In the case of 15 and 20 wt%, where LIG pores and flakes were covered by PEDOT:PSS, conductivities increased to 164.2 Scm^{-1} (~17.4 Ω/sq.), and 214.8 Scm^{-1} (~13.3Ω/sq.), respectively. However, Crack analysis was performed for the 15 and 20 wt% samples after 100 bendings. The maximum bending angle was approximately 150°, as illustrated in Fig. 3B. The microscopic images of the 15 and 20 wt% samples after 100 bendings are shown in Fig. S10. It was found that the conductivity of the 15 wt% sample remained largely unchanged, as it did not crack during bending (Fig. S10A). On the other hand, the conductivity of the 20 wt% sample decreased to 149.58 Scm−1 (~19.1 Ω/sq.), as a result of cracks, introduced during repeated bending, as illustrated in Fig. S10B.

3.3. Electrochemical characterization of the modified LIG electrodes

Electrochemical characteristics of the developed electrodes were analyzed by CV and EIS. The electrochemical performances for optimizing the weight ratio of PEDOT:PSS and the number of CV segments for Pt@Pd electroplating are detailed in chapter S 3.2 (Figs. S11 and S12). The CV curves of bare LIG, Pt@Pd/LIG, PP/LIG, and Pt@Pd/PP/LIG measured in 5 mM $K_3[Fe(CN)_6]$ are shown in Fig. 3C. The CV area of the Pt@Pd/PP/LIG electrode was the highest, indicating superior electrocatalytic activity. Furthermore, the effective surface areas of the various electrodes were calculated from the CV curves using the Randles-Sevick equation (Zahed et al., 2019).

$$I_P = 2.69 \times 10^5 A D^{1/2} n^{3/2} \gamma^{1/2} C \quad (2)$$

Where, n is the number of electrons participating in the redox reaction, D is the diffusion coefficient of the electrolyte ($6.7 \pm 0.02 \times 10^{-6} cm^2/s$), C is the concentration of the electrolyte (mol/L), γ is the scan rate (Vs^{-1}). The electroactive surface area (A) of the bare electrode is 0.31 cm^2, and that for the PP/LIG is 0.38 cm^2. The electrodeposition of Pt@Pd nanoparticles onto PP/LIG further increased the effective surface area (0.84 cm^2) as well as the electron transfer rate. The synergistic effect of bimetallic nanoparticles is discussed in detail in S 3.3 (Fig. S13).

The interfacial properties of electrodes were investigated by electrochemical impedance measurements. Fig. 3D presents the EIS spectra of the modified electrodes: bare LIG, Pt@Pd/LIG, PP/LIG, and Pt@Pd/PP/LIG, tested using the 5 mM $Fe(CN)_6^{3-}$ redox probe. The inset figure represents the Randles equivalent circuit model used to fit experimental results. In this circuit, R_s, R_{ct}, and CPE represent the solution resistance, electron transfer resistance, and constant phase element, respectively. The semicircle diameter of the Nyquist plot corresponds to the charge transfer resistance (R_{ct}). All modified electrodes demonstrated distinct

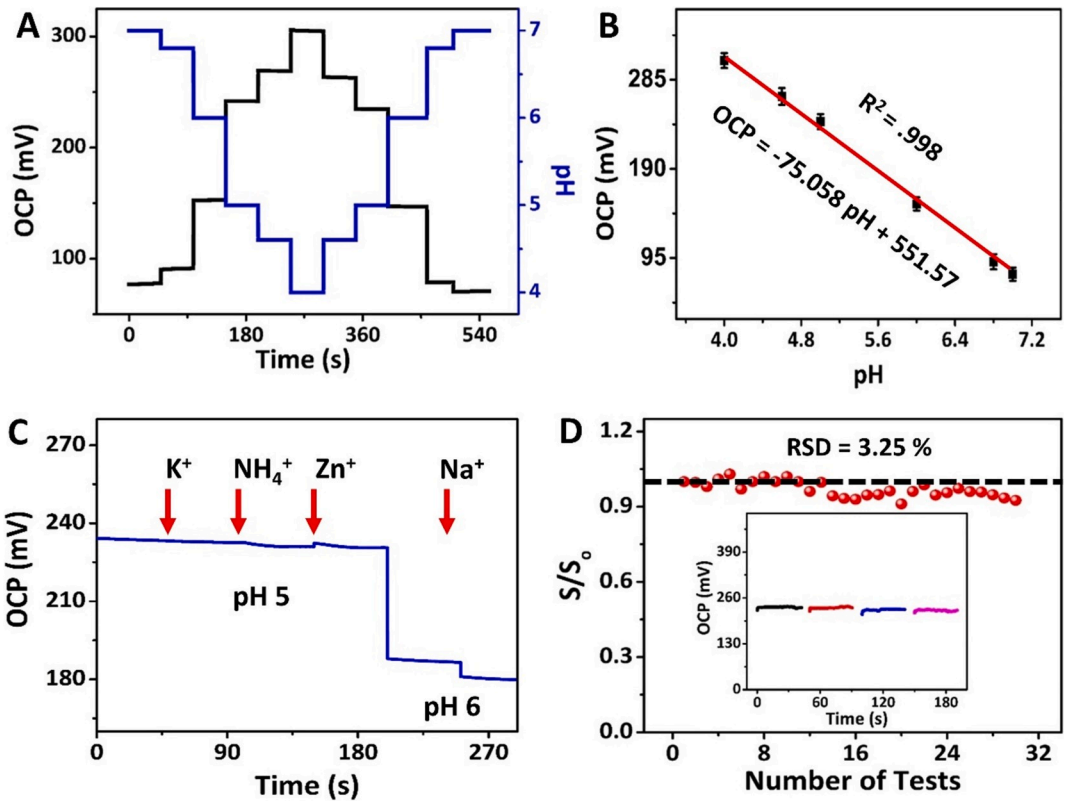

Fig. 5. Electrochemical investigation of the fabricated pH sensor. A) OCP versus time curves for buffer solutions with a pH range from 4 to 7, including a reversibility test, B) Calibration plot of the pH sensor, C) Selectivity test of the pH sensor, D) Relative responses (S/S_0) were calculated by the ratio of instant OCPs (S) to initial OCPs (S_0) with 30 iterations (the inset figure showing OCPs at 1st, 10th, 20th, 30th, tests).

diameter semicircles, indicating differing R_{ct}. The R_{ct} values for bare LIG, Pt@Pd/LIG, PP/LIG, and Pt@Pd/PP/LIG were 335.2Ω, 299.6Ω, 126.2Ω, and 119.8Ω, respectively. The low R_{ct} value of 119.8Ω obtained for Pt@Pd/PP/LIG, implies superior electron transfer properties compared to that of other electrodes.

3.4. Electrochemical investigation of the fabricated glucose biosensor

Fig. 4 represents the electrochemical performance of the fabricated glucose biosensor. The working mechanism of the biosensor is schematically described in Fig. 1(IV). The electrocatalytic oxidation of glucose and the effect of scan rates on the biosensor are discussed in chapter S 3.4 (Fig. S14). Fig. 4A contains the chronoamperometry curve for the successive injection of glucose into the 0.1 M PBS (pH = 7.4). The concentration of glucose injected was in the range of 3 μM–9.2 mM. Fig. 4B shows the calibration plot obtained from the anodic current responses with a correlation coefficient (R^2) of 0.996 and an excellent sensitivity of 247.3 $\mu A/mM^{-1}/cm^{-2}$. The LOD was calculated to be 3 μM, using the formula LOD = $3S_b/S$ (where S_b is the standard deviation of the blank signal, and S is the sensitivity) (Mani et al., 2016). The response of the biosensor for 1 mM glucose reached a steady-state within 3.6 s, which is regarded as the response time (Fig. S15).

Besides, Fig. 4C illustrates the selectivity test of the biosensor to determine 0.1 mM glucose in the presence of interference molecules: 0.1 mM acetaminophen, 0.1 mM urea, 10 μM ascorbic acid, 2 μM uric acid, 1 mM KCl, 10 mM NaCl, and 5 mM lactate. The sensor did not respond with any significant signals to the injection of interference molecules, exhibiting good selectivity for glucose. Fig. 4D lists 30 relative responses to 1 mM glucose with the same biosensor, calculated by the ratio of instant current to initial current (S/S_0) (RSD = 2.13%). The inset figure shows substantially higher current responses for the 1st, 10th, 20th, and 30th test. This behavior would reduce any interference by background noise, as well as uphold the sensitivity for a longer period. The reproducibility test and the effect of temperature on the biosensor are described in chapter S 3.5 (Fig. S16). Based on the analyses, the biosensor exhibited a sensing performance comparable to other state-of-the-art glucose biosensors, as detailed in Table S3.

3.5. Electrochemical investigation of the fabricated pH sensor

Fig. 5 illustrates the electrochemical performance of the fabricated pH sensor under ambient conditions. The fabricated reference electrode was calibrated against commercial Ag/AgCl (3M KCl). The potential shift of the fabricated electrode was approximately 150 mV, as seen in Fig. S17. The sensing performance was monitored in terms of open circuit potential (OCP) vs time. Fig. 5A depicts the OCP values with the variation in pH of standard buffer solutions, for increasing and decreasing pHs, ranging from 4 to 7 and 7 to 4. This experiment proved the reversibility of the pH sensor. The sensor yielded a linear response with an excellent sensitivity of 75.06 mV/pH, and a high regression coefficient (R^2 = 0.998), as evident in Fig. 5B. The sensitivity was calculated from the slope of the calibration curve, which exceeded the Nernst limit. It has been reported that the sensitivity depends on the phases of PANI and the electrode manufacturing process (Kulkarni and Kale, 2014). Therefore, the reason for the high sensitivity of the pH sensor exceeding the Nernst limit was likely due to the effective electropolymerization of aniline on the highly conductive electrode of PP/LIG.

Fig. 5C shows the selectivity results of the pH sensor in the presence of other ions, including K^+, NH_4^+, $Zn^{+,}$ and Na^+. There were no significant changes in OCPs for other ions, as hydrogen ions were detected by deprotonation on the PANI modified electrode. Fig. 5D shows the relative responses for 30 successive measurements in pH 6 buffer solution using the same pH sensor. The inset figure shows OCP responses for the

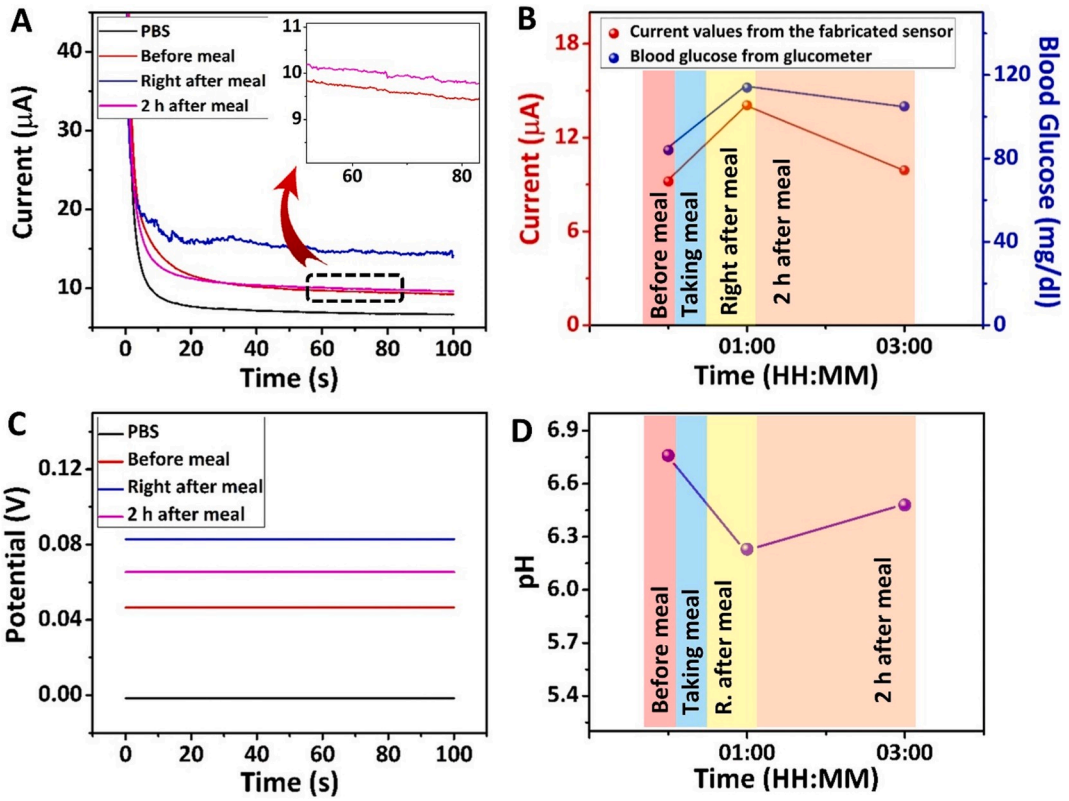

Fig. 6. Performance of the biosensor for pH and glucose detection in sweat. A) Chronoamperometric response obtained directly from three different sweat samples (Before meal, Right after meal, 2 h after meal) and 0.1 M PBS solution, B) Comparison of the current values obtained from the fabricated sensor with the blood glucose levels measured with a commercial glucometer with respect to exercise time, C) OCP responses obtained directly from three different sweat samples (Before meal, Right after meal, 2 h after meal) and 0.1 M PBS solution, D) Variation of pH values with meal ingestion and exercise time.

1st, 10th, 20th, and 30th tests. The net potentials of OCP signals and the sensitivity were substantially higher compared to other reported pH sensors (Table S4). The reproducibility test and the effect of temperature on the pH sensor are described in chapter S 3.6 (Fig. S18). The above results indicate that the developed sensor is capable of valid pH analysis.

3.6. Real sample analysis

The feasibility of the biosensor was verified by its application for monitoring human perspiration. Fig. 6 represents the performance of the biosensor for sweat glucose and pH detection. The subject had perspired during physical exercise and collected a few hundred microliters of sweat under three different conditions: before meal, right after meal, and 2 h after meal (Fig. S19A). Before every perspiration event, the subject's blood glucose concentration was measured using a conventional glucometer. Fig. S19B is an optical image of the experimental set-up with a sweat drop of 200 μL on the as-developed biosensor. Fig. 6A displays the chronoamperometric responses obtained directly from 200 μL of sweat and 0.1 M PBS. The current response in the 0.1 M PBS buffer was significantly lower because it contained fewer constituents, unlike sweat. Notably, the glucose biosensor exhibited a distinct increased current response for the after-meal sweat sample, as compared to the before-meal sweat sample. In addition, the response for the 2 h after-meal sweat sample decreased compared to that of the right after meal sample. The blood glucose level increased immediately following a meal due to the immediate release of insulin and amylin into the bloodstream, and subsequently decreased with time. Sweat glucose followed a similar trend, as evident in Fig. 6B. Furthermore, the sweat pH values also varied (Fig. 6C and D), due to the rate of excretion of lactic acid during exercise before and after meal. The sweat glucose concentration could be corrected for the effects of pH before and after meal ingestion.

4. Conclusion

As a novel class of multifunctional material, LIG was successfully rendered mechanically robust and highly conductive by the spray-coating of PEDOT:PSS on its surface. This flexible substrate was further modified with Pt@Pd nanoparticles for glucose detection, and with PANI for pH detection. The biosensor exhibited high sensitivity and clinical linearity for both glucose and pH detection. Besides, it also exhibited excellent flexing stability and highly selective sensing of glucose and pH. The variation of glucose and pH concentration in perspiration upon meal ingestion and exercise was successfully monitored. This work revealed a promising basis for developing other flexible biosensors for monitoring important physiological compounds in perspiration. Furthermore, the proposed biosensor can be integrated with a flexible printed circuit board to develop a miniaturized sweat monitoring system.

Declaration of competing interest

The authors declare that they have no known competing financial interests or personal relationships that could have appeared to influence the work reported in this paper.

CRediT authorship contribution statement

Md Abu Zahed: Conceptualization, Formal analysis, Writing - original draft, Validation. **Sharat Chandra Barman:** Investigation, Writing - original draft. **Partha Sarati Das:** Visualization, Writing - original draft. **Md Sharifuzzaman:** Writing - review & editing. **Hyo Sang Yoon:** Formal analysis, Methodology. **Sang Hyuk Yoon:** Methodology. **Jae Yeong Park:** Funding acquisition, Supervision.

Acknowledgment

This research was supported by the Technology Innovation Program (20000773, Development of nanomultisensors based on wearable patch for nonhaematological monitoring of metabolic syndrome) by the Ministry of Trade, Industry & Energy (MI, South Korea), the Bio & Medical Technology Development Program of the NRF grant funded by the Korean government (MSIT) (NRF-2017M3A9F1031270).

Appendix A. Supplementary data

Supplementary data to this article can be found online at https://doi.org/10.1016/j.bios.2020.112220.

References

Abellán-Llobregat, A., Jeerapan, I., Bandodkar, A., Vidal, L., Canals, A., Wang, J., Morallón, E., 2017. A stretchable and screen-printed electrochemical sensor for glucose determination in human perspiration. Biosens. Bioelectron. 91, 885–891. https://doi.org/10.1016/j.bios.2017.01.058.

Bandodkar, A.J., Hung, V.W.S., Jia, W., Valdés-Ramírez, G., Windmiller, J.R., Martinez, A.G., Ramírez, J., Chan, G., Kerman, K., Wang, J., 2013. Tattoo-based potentiometric ion-selective sensors for epidermal pH monitoring. Analyst 138, 123–128. https://doi.org/10.1039/c2an36422k.

Bandodkar, A.J., Jeerapan, I., Wang, J., 2016. Wearable chemical sensors: present challenges and future prospects. ACS Sens. 1, 464–482. https://doi.org/10.1021/acssensors.6b00250.

Barman, S.C., Zahed, M.A., Sharifuzzaman, M., Ko, S.G., Yoon, H., Nah, J.S., Xuan, X., Park, J.Y., 2020. A polyallylamine anchored amine-rich laser-ablated graphene platform for facile and highly selective electrochemical IgG biomarker detection. Adv. Funct. Mater. 1–10. https://doi.org/10.1002/adfm.201907297, 1907297.

Brugarolas, R., Latif, T., Dieffenderfer, J., Walker, K., Yuschak, S., Sherman, B.L., Roberts, D.L., Bozkurt, A., 2016. Wearable heart rate sensor systems for wireless canine health monitoring. IEEE Sensor. J. 16, 3454–3464. https://doi.org/10.1109/JSEN.2015.2485210.

Choe, J.E., Ahmed, M.S., Jeon, S., 2015. 3,4-Ethylenedioxythiophene functionalized graphene with palladium nanoparticles for enhanced electrocatalytic oxygen reduction reaction. J. Power Sources 281, 211–218. https://doi.org/10.1016/j.jpowsour.2015.01.176.

Collaborators, Naset, 1991. The New England Journal of Medicine Downloaded from nejm.org on March 29, 2011. For personal use only. No other uses without permission. N. Engl. J. Med. 329, 977–986. https://doi.org/10.1056/NEJM199309303291401.

del Agua, I., Mantione, D., Ismailov, U., Sanchez-Sanchez, A., Aramburu, N., Malliaras, G. G., Mecerreyes, D., Ismailova, E., 2018. DVS-crosslinked PEDOT:PSS free-standing and textile electrodes toward wearable health monitoring. Adv. Mater. Technol. 3, 1–8. https://doi.org/10.1002/admt.201700322.

Du, F., Cao, N., Zhang, Y., Fu, P., Wu, Y., Lin, Z., 2018. PEDOT : PSS/graphene quantum dots films with enhanced thermoelectric properties via strong interfacial interaction and phase separation. Sci. Rep. 1–12. https://doi.org/10.1038/s41598-018-24632-4.

Ferrari, A.C., Meyer, J.C., Scardaci, V., Casiraghi, C., Lazzeri, M., Mauri, F., Piscanec, S., Jiang, D., Novoselov, K.S., Roth, S., Geim, A.K., 2006. Raman spectrum of graphene and graphene layers. Phys. Rev. Lett. 187401, 1–4. https://doi.org/10.1103/PhysRevLett.97.187401.

Gao, W., Emaminejad, S., Nyein, H.Y.Y., Challa, S., Chen, K., Peck, A., Fahad, H.M., Ota, H., Shiraki, H., Kiriya, D., Lien, D.H., Brooks, G.A., Davis, R.W., Javey, A., 2016. Fully integrated wearable sensor arrays for multiplexed in situ perspiration analysis. Nature 529, 509–514. https://doi.org/10.1038/nature16521.

Guangyuan Xu, Z.A.J., Desprez, V., Kilmartina, P.A., Travas-Sejdic, J., 2018. Sensitive, selective, disposable electrochemical dopamine sensor based on PEDOT-modified laser scribed graphene _ Elsevier Enhanced Reader.pdf. Biosens. Bioelectron. 107, 184–191.

Guo, H., Lan, C., Zhou, Z., Sun, P., Wei, D., Li, C., 2017. Transparent, flexible, and stretchable WS 2 based humidity sensors for electronic skin. Nanoscale 9, 6246–6253. https://doi.org/10.1039/c7nr01016h.

Guo, X., Jian, J., Lin, L., Zhu, H., Zhu, S., 2013. O2 plasma-functionalized SWCNTs and PEDOT/PSS composite film assembled by dielectrophoresis for ultrasensitive trimethylamine gas sensor. Analyst 138, 5265–5273. https://doi.org/10.1039/c3an36690a.

Guo, Y., Otley, M.T., Li, M., Zhang, X., Sinha, S.K., Treich, G.M., Sotzing, G.A., 2016. PEDOT:PSS "wires" printed on textile for wearable electronics. ACS Appl. Mater. Interfaces 8, 26998–27005. https://doi.org/10.1021/acsami.6b08036.

Hossain, M.F., Park, J.Y., 2015. An enzymatic hybrid electrode platform based on chemically modified reduced graphene oxide decorated with palladium and platinum alloy nanoparticles for biosensing applications. J. Electrochem. Soc. 162, B185–B192. https://doi.org/10.1149/2.0951507jes.

Imani, S., Bandodkar, A.J., Mohan, A.M.V., Kumar, R., Yu, S., Wang, J., Mercier, P.P., 2016. A wearable chemical-electrophysiological hybrid biosensing system for real-time health and fitness monitoring. Nat. Commun. https://doi.org/10.1038/ncomms11650.

Jiang, X., Wang, Z., Han, W., Liu, Q., Lu, S., Wen, Y., Hou, J., Huang, F., Peng, S., He, D., Cao, G., 2017. High performance silicon-organic hybrid solar cells via improving conductivity of PEDOT:PSS with reduced graphene oxide. Appl. Surf. Sci. 407, 398–404. https://doi.org/10.1016/j.apsusc.2017.02.193.

Kim, S.M., Kim, C.H., Kim, Y., Kim, N., Lee, W.J., Lee, E.H., Kim, D., Park, S., Lee, K., Rivnay, J., Yoon, M.H., 2018. Influence of PEDOT:PSS crystallinity and composition on electrochemical transistor performance and long-term stability. Nat. Commun. 9 https://doi.org/10.1038/s41467-018-06084-6.

Kulkarni, M.V., Kale, B.B., 2014. Erratum: studies of conducting polyaniline (PANI) wrapped-multiwalled carbon nanotubes (MWCNTs) nanocomposite and its application for optical pH sensing (Sensors and Actuators, B: chemical (2013) 187 (407-412)). Sensor. Actuator. B Chem. 197, 422. https://doi.org/10.1016/j.snb.2014.03.045.

Kurra, N., Jiang, Q., Nayak, P., Alshareef, H.N., 2019. Laser-derived graphene: a three-dimensional printed graphene electrode and its emerging applications. Nano Today 24, 81–102. https://doi.org/10.1016/j.nantod.2018.12.003.

Lee, J., Choi, W., 2015. Surface modification of sulfur cathodes with PEDOT:PSS conducting polymer in lithium-sulfur batteries. J. Electrochem. Soc. 162, A935–A939. https://doi.org/10.1149/2.0651506jes.

Lei, Y., Zhao, W., Zhang, Y., Jiang, Q., He, J.H., Baeumner, A.J., Wolfbeis, O.S., Wang, Z. L., Salama, K.N., Alshareef, H.N., 2019. A MXene-based wearable biosensor system for high-performance in vitro perspiration analysis. Small 15, 1–10. https://doi.org/10.1002/smll.201901190.

Li, G., Wang, X., Yan, L., Wang, Y., Zhang, Z., Xu, J., 2019. PdPt bimetal-functionalized SnO2 nanosheets: controllable synthesis and its dual selectivity for detection of carbon monoxide and methane. ACS Appl. Mater. Interfaces 11, 26116–26126. https://doi.org/10.1021/acsami.9b08408.

Lin, J., Peng, Z., Liu, Y., Ruiz-zepeda, F., Ye, R., Samuel, E.L.G., Yacaman, M.J., Yakobson, B.I., Tour, J.M., 2014. Commercial polymers. Nat. Commun. 5, 5–12. https://doi.org/10.1038/ncomms6714, 5714.

Links, D.A., 2012. Thermoelectric properties of nanocomposite thin films prepared with poly(3,4-ethylenedioxythiophene) poly(styrenesulfonate) and graphene. Phys. Chem. Chem. Phys. 14, 3530–3536. https://doi.org/10.1039/c2cp23517j.

Liu, Y., Weng, B., Razal, J.M., Xu, Q., Zhao, C., Hou, Y., Seyedin, S., Jalili, R., Wallace, G. G., Chen, J., 2015. High-performance flexible all-solid-state supercapacitor from large free-standing graphene-PEDOT/PSS films. Sci. Rep. 5, 1–11. https://doi.org/10.1038/srep17045.

Mani, S., Vediyappan, V., Chen, S.M., Madhu, R., Pitchaimani, V., Chang, J.Y., Liu, S. Bin, 2016. Hydrothermal synthesis of NiWO4 crystals for high performance non-enzymatic glucose biosensors. Sci. Rep. 6, 2–9. https://doi.org/10.1038/srep24128.

Matzeu, G., Florea, L., Diamond, D., 2015. Advances in wearable chemical sensor design for monitoring biological fluids. Sensor. Actuator. B Chem. 211, 403–418. https://doi.org/10.1016/j.snb.2015.01.077.

Merche, D., Hubert, J., Poleunis, C., Yunus, S., Bertrand, P., De Keyzer, P., Reniers, F., 2010. One step polymerization of sulfonated polystyrene films in a dielectric barrier discharge. Plasma Process. Polym. 7, 836–845. https://doi.org/10.1002/ppap.201000024.

Moyer, J., Wilson, D., Finkelshtein, I., Wong, B., Potts, R., 2012. Correlation between sweat glucose and blood glucose in subjects with diabetes. Diabetes Technol. Therapeut. 14, 398–402. https://doi.org/10.1089/dia.2011.0262.

Munje, R.D., Muthukumar, S., Prasad, S., 2017. Lancet-free and label-free diagnostics of glucose in sweat using Zinc Oxide based flexible bioelectronics. Sensor. Actuator. B Chem. 238, 482–490. https://doi.org/10.1016/j.snb.2016.07.088.

Nayak, P., Kurra, N., Xia, C., Alshareef, H.N., 2016. Highly efficient laser scribed graphene electrodes for on-chip electrochemical sensing applications. Adv. Electron. Mater. 2 https://doi.org/10.1002/aelm.201600185.

Newman, J.D., Turner, A.P.F., 2005. Home blood glucose biosensors: a commercial perspective. Biosens. Bioelectron. 20, 2435–2453. https://doi.org/10.1016/j.bios.2004.11.012.

Nyein, H.Y.Y., Gao, W., Shahpar, Z., Emaminejad, S., Challa, S., Chen, K., Fahad, H.M., Tai, L.C., Ota, H., Davis, R.W., Javey, A., 2016. A wearable electrochemical platform for noninvasive simultaneous monitoring of Ca2+ and pH. ACS Nano 10, 7216–7224. https://doi.org/10.1021/acsnano.6b04005.

Patil, S., Ghadi, H., Ramgir, N., Adhikari, A., Rao, V.R., 2019. Monitoring soil pH variation using Polyaniline/SU-8 composite film based conductometric microsensor. Sensor. Actuator. B Chem. 286, 583–590. https://doi.org/10.1016/j.snb.2019.02.016.

Patterson, M.J., Galloway, S.D.R., Nimmo, M.A., 2000. Variations in regional sweat composition in normal human males. Exp. Physiol. 85, 869–875. https://doi.org/10.1111/j.1469-445X.2000.02058.x.

Schmid-Wendtner, M.H., Korting, H.C., 2006. The pH of the skin surface and its impact on the barrier function. Skin Pharmacol. Physiol. 19, 296–302. https://doi.org/10.1159/000094670.

Semwal, V., Gupta, B.D., 2019. Highly sensitive surface plasmon resonance based fiber optic pH sensor utilizing rGO-Pani nanocomposite prepared by in situ method. Sensor. Actuator. B Chem. 283, 632–642. https://doi.org/10.1016/j.snb.2018.12.070.

Setti, L., Fraleoni-Morgera, A., Ballarin, B., Filippini, A., Frascaro, D., Piana, C., 2005. An amperometric glucose biosensor prototype fabricated by thermal inkjet printing. Biosens. Bioelectron. 20, 2019–2026. https://doi.org/10.1016/j.bios.2004.09.022.

Sharifuzzaman, M., Barman, S.C., Rahman, M.T., Zahed, M.A., Xuan, X., Park, J.Y., 2019. Green synthesis and layer-by-layer assembly of amino-functionalized graphene oxide/carboxylic surface modified trimetallic nanoparticles nanocomposite for label-free electrochemical biosensing. J. Electrochem. Soc. 166, B983–B993. https://doi.org/10.1149/2.0821912jes.

Sonner, Z., Wilder, E., Heikenfeld, J., Kasting, G., Beyette, F., Swaile, D., Sherman, F., Joyce, J., Hagen, J., Kelley-Loughnane, N., Naik, R., 2015. The microfluidics of the eccrine sweat gland, including biomarker partitioning, transport, and biosensing implications. Biomicrofluidics 9, 1–19. https://doi.org/10.1063/1.4921039.

Takamatsu, S., Lonjaret, T., Crisp, D., Badier, J.M., Malliaras, G.G., Ismailova, E., 2015. Direct patterning of organic conductors on knitted textiles for long-term electrocardiography. Sci. Rep. 5, 1–7. https://doi.org/10.1038/srep15003.

Whiting, D.R., Guariguata, L., Weil, C., Shaw, J., 2011. IDF Diabetes Atlas: global estimates of the prevalence of diabetes for 2011 and 2030. Diabetes Res. Clin. Pract. 94, 311–321. https://doi.org/10.1016/j.diabres.2011.10.029.

Zahed, A., Barman, S.C., Toyabur, R.M., Xuan, X., Nah, J., Park, J.Y., 2019. Ex situ hybridized hexagonal cobalt oxide nanosheets and RGO @ MWCNT based nanocomposite for ultra-selective electrochemical detection of ascorbic acid , dopamine , and uric acid. J. ofThe Electrochem. Soc. 166, 304–311. https://doi.org/10.1149/2.0131906jes.

Zhang, J., Sasaki, K., Sutter, E., Adzic, R.R., 2007. Stabilization of platinum oxygen-reduction electrocatalysts using gold clusters. Science 84 315, 220–222. https://doi.org/10.1126/science.1134569.

Zhang, S., Shao, Y., Yin, G., Lin, Y., 2010. Electrostatic self-assembly of a pt-around-au nanocomposite with high activity towards formic acid oxidation. Angew. Chem. Int. Ed. 49, 2211–2214. https://doi.org/10.1002/anie.200906987.

Zhang, Z., Song, M., Hao, J., Wu, K., Li, C., Hu, C., 2018. Visible light laser-induced graphene from phenolic resin: a new approach for directly writing graphene-based electrochemical devices on various substrates. Carbon N. Y. 127, 287–296. https://doi.org/10.1016/j.carbon.2017.11.014.